Interaction of a Synthetic Jet with a Flat Plate Boundary Layer

R. Mittal[1] P. Rampunggoon[2]
Department of Mechanical Engineering
University of Florida
Gainesville, Florida, 32611

H. S. Udaykumar[3]
Department of Mechanical Engineering
University of Iowa
Iowa City, Iowa, 52242

ABSTRACT

The interaction of a modeled synthetic jet with a flat plate boundary layer is investigated numerically using an incompressible Navier–Stokes solver. The diaphragm is modeled in a realistic manner as a moving boundary in an effort to accurately compute the flow inside the jet cavity. The primary focus of the current study is on describing the dynamics of the synthetic jet in the presence of external crossflow. A systematic parametric study has been carried out where the diaphragm amplitude, external flow Reynolds number and slot dimensions are varied. The simulations allow us to extract some interesting flow physics associated with the vortex dynamics of the jet and also provide insight into the scaling of the performance characteristics of the jet with these parameters.

1. INTRODUCTION

The synthetic jet has emerged as one of the most useful micro (or meso) fluidic devices with the potential application ranging from thrust vectoring of jet engines (Smith et al. 1997), mixing enhancement (Chen et al. 1999, Davis et al. 1999) to active control of separation and turbulence in boundary layers (Smith & Glezer 1998, Crook et al. 1999). The utility of these devices in controlling separation has for the most part, been demonstrated in laboratory setups only, and a number of issues need to be addressed in order to transition this technology to practical applications. First, the performance of a synthetic jet actuator depends on a number of geometrical, structural and flow parameter and there is a little understanding as to how this performance scales with these parameters. Such an understanding would be a critical element in the sizing, design and deployment of these actuators. Secondly, although experiments have shown that for instance, synthetic jets can be used to delay separation (Amitay et al. 1997), our understanding of the physical mechanisms that lead to this effect is quite limited. Both of these issues can be addressed by a systematic parameter study of a synthetic jet. In the current study we have used numerical simulations to perform a detailed parametric study of a simplified configuration which includes a two-dimensional synthetic jet interacting with a flat plate boundary layer.

[1]Assistant Professor
[2]Graduate Student
[3]Assistant Professor

2. FLOW CONFIGURATION AND SIMULATION APPROACH

Flow Configuration

Consider the two-dimensional synthetic jet device in Figure 1, which is attached beneath a flat plate on which develops a laminar Blasius boundary layer. The synthetic jet is created at the slot by the oscillation of a diaphragm attached to the bottom of the jet cavity and the diaphragm deflection is characterized by the deflection amplitude (A) and angular frequency (ω). The cavity, which is rectangular in shape is defined by the cavity width (W) and the cavity height (H). A slot type exit is chosen for the jet and this orifice is characterized by a height (h) and width (d). The exterior flow which consists of a laminar Blasius boundary layer is characterized by a freestream velocity (U_∞) and boundary layer thickness (δ). Finally, the fluid is characterized by its kinematic viscosity (ν) and density (ρ).

Additional parameters need to be considered in the situation where compressibility effects inside the cavity become significant. However, from the point of view of device efficiency, it might be advantageous to operate in the incompressible flow regime and this can be easily accomplished by detuning the diaphragm frequency from the acoustic resonance frequency of the cavity. Therefore, with the underlying assumption that actual devices will be designed to operate in the incompressible flow regime, in the current study, we also focus only on this regime.

Jet Characterization and Scaling

The flow emerging from the slot is in principle a function of all the parameters described in the paragraph above. The exit flow which is both a function of space and time, can be characterized through a number of different parameters. In many previous studies, a parameter considered key to characterizing the jet in the presence of an exterior flow is the momentum

coefficient (Amitay et al. 1998, Seifert et al. 1996) which is the net momentum imparted by the jet over one cycle normalized by the momentum flux of the external flow. However, it is not clear that this or any other single parameter would be sufficient to characterize the dynamics associated with the complex jet. Thus, even the choice of parameters that would adequately characterize the jet in the presence of external crossflow is an open question.

In the current study a more general approach to characterizing the jet behavior, which employs the successive moments of the jet velocity profile, is advocated. The n^{th} moment of the jet $\left(C^n_{\phi_{12}}\right)$ is defined as

$$C^n_{\phi_{12}} = \frac{1}{\phi_2 - \phi_1}\frac{1}{d}\int_{\phi_1}^{\phi_2}\int_{-d/2}^{d/2}[V_J(x,\phi)]^n dx\, d\phi \qquad (1)$$

where V_J is the jet velocity normalized by a suitable velocity scale (freestream velocity or inviscid jet velocity). Our preliminary simulations indicate that the jet flow is significantly different in the ingestion and expulsion phases and characterizing this difference is critical to understanding the physics of this flow. Thus, it is natural to define the moment separately for the ingestion and expulsion phases and these are denoted by C^n_{in} and C^n_{ex} respectively. This hierarchical characterization in terms of the moments of the velocity profile is extremely useful since it provides a systematic framework for the development of scaling laws. Furthermore, this type of characterization is not simply for mathematical convenience since a number of these moments have direct physical significance. For instance $\left(C^1_{in} + C^1_{ex}\right)$ corresponds to the jet mass flux (which is identically equal to zero for a synthetic jet) and C^1_{ex} is the mean normalized jet velocity during the expulsion phase. Furthermore, $\left(C^2_{ex} + C^2_{in}\right)$ and $\left(C^3_{in} + C^3_{ex}\right)$ correspond to the normalized momentum and kinetic energy fluxes of the jet. This last quantity is also a measure of the asymmetry of the flow during the expulsion and ingestion phases. Finally for $n = \infty$, $\left(C^n_{ex}\right)^{1/n}$ represents the normalized maximum jet exit velocity.

With the jet characteristic parameters chosen in this manner, the question now is to determine their dependence on the flow and geometrical parameters of this configuration. Using the Buckingham Pi theorem, this functional dependence can be written in terms of non–dimensional parameters as:

$$\left(C_{in}{}^n; C_{ex}{}^n\right) = fn\left(\frac{W}{H}, \frac{A}{H}, \frac{d}{h}, \frac{d}{W}, \sqrt{\frac{\omega d^2}{\nu}}, \frac{U_\infty \delta}{\nu}, \frac{\delta}{d}\right) \qquad (2)$$

where

W/H : width to height ratio of cavity

A/H : diaphragm amplitude to cavity height ratio

d/h : orifice width to height ratio

d/W : orifice width to cavity width ratio

$\sqrt{\omega d^2/\nu} = S$: Stokes number

$U_\infty \delta/\nu = \mathrm{Re}_\delta$: boundary layer thickness Reynolds number

δ/d : ratio of boundary layer thickness to slot width.

It is worth noting that the first five parameters on the RHS of Equation (2) depend only on the synthetic jet device, whereas the last two parameters depend on the outer boundary layer. The first objective of a scaling analysis would then be to determine the functional dependence denoted in Equation (2). From previous studies, it is clear that the moment coefficients will depend on the jet and slot parameters. However, it is not clear what effect the exterior flow parameters have on the jet flow and the flow in the cavity. This requires accurate simulation of the flow inside the jet cavity and this is one objective of the current study. In the past, the diaphragm has been modeled by assuming a piston–like motion (Rizzetta et al. 1998) and this can lead to a significantly different flow inside the cavity. In the current simulations, the diaphragm is modeled in a more realistic manner as a plate oscillating in its fundamental mode. Thus the diaphragm has its maximum deflection at the center and zero deflection at the two ends.

Clearly, the parameter space of this flow configuration is enormous and difficult to cover in any single investigation. We therefore focus on the parameters that are expected to have a strong influence on the characteristics of the jet. The parameters to be varied in the current study are the diaphragm amplitude (*A/H*), orifice width to height ratio (*d/h*) and the boundary layer thickness Reynolds number of the external flow (Re_δ). In addition to this, the Stokes number and δ/d have also been varied but those results are not included in the current paper. These parameters are chosen because preliminary simulations indicated significant variation in the jet with these parameters and it was therefore expected that useful insight into the physics of this flow could be gained by varying these parameters. The values of the other parameters are fixed at *W/H*=5, *d/W*=0.05, δ/d=2 and furthermore, all results presented here correspond to a Stokes number of 10.

One parameter found useful in the normalization of the jet velocity is the maximum inviscid jet velocity ($V^{inv}_{\max}$) which, for the prescribed diaphragm motion is given by

$$V^{inv}_{\max} = \frac{AW\omega}{2d} \qquad (3)$$

Simulation Approach

A previously developed Cartesian grid solver (Udaykumar et al. 1999, Ye et al. 1999, Udaykumar et al. 2000) is being employed in these simulations. Details of the solution procedure can be found in these papers. This solver allows simulation of unsteady viscous incompressible flows with complex immersed moving boundaries on Cartesian grids. Thus, the grid does not need to conform to the complex moving boundaries and this simplifies the gridding of the flow domain. The solver employs a second–order accurate central–difference scheme for spatial discretization and a mixed explicit–implicit fractional step scheme for time advancement. An efficient multigrid algorithm is used for the solving the pressure Poisson equation.

The key advantage of this solver for the current flow is that the entire geometry of the synthetic jet including the oscillating diaphragm is modeled on the stationary Cartesian mesh. Figure 2 shows the typical mesh used in the current simulations. As the diaphragm moves over the underlying Cartesian mesh, the

discretization in the cells cut by the solid boundary is modified to account for the presence of the solid boundary. In addition, suitable boundary conditions also need to be prescribed for the external flow. For the quiescent external flow case, a soft velocity boundary condition (corresponding to homogeneous Neumann condition) is applied on the north, east and west boundaries. In the simulations with an external cross–flow, the Blasius boundary layer profile is prescribed on the west boundary and a uniform freestream velocity prescribed on the north boundary which is located more than 40*d* away from the slot. On the east boundary, a soft boundary condition is applied which allows vortex structures to convect out of the domain with minimal distortion and reflections.

All simulations are run for a few cycles until a steady state is reached. The simulations are then continued over at least five cycles beyond this stage and statistics accumulated over this time interval. Thus, all results presented here correspond to the stationary state of the flow.

3. DISCUSSION OF RESULTS

In this section, we describe the vortex dynamics observed for some selected cases. For ease of comparison, all cases discussed in the following section, unless otherwise noted, correspond to *A/H*=0.1 and *h/d*=1.0

Quiescent External Flow

Case 1 (Re_δ = 0*)* This case corresponds to a quiescent external flow which has been studied extensively in the past by other groups (James et al. 1996, Kral et al. 1997, Rizzetta et al. 1998). Figure 3 shows a sequence of contour plots of spanwise vorticity plots for this case. At the maximum expulsion stage (when the diaphragm is moving up with the maximum velocity), a pair of counter rotating vortices forms at the orifice. This vortex pair is removed from the surface by its own induced velocity. As the diaphragm moves down, it entrains external fluid through the slot. However, since the vortices have already traveled away from the orifice, they are not affected by the motion of the entrained fluid. Another pair of vortices generated inside the cavity during the downstroke sets up a complex flow inside the cavity. However, for this simulation, the flow inside the cavity remains symmetric about the vertical centerline. There is also a large region of almost stagnant fluid near the two side walls of the cavity. Currently it is not clear what effect this stagnant fluid has on the jet flow. However, it should be pointed out that in these regions especially, the flow produced by a piston–like motion of the diaphragm would be quite different.

Case 2 (Re_δ = 0, and *A/H* = 0.1 *h/d* =3) Comparison of this case with Case 1 allows us to gauge in a limited manner, the effect of the *h/d* parameter. The sequence of vorticity contour plots over one cycle is shown in Figure 4. In general it is found that for this particular set of parameters, the flow outside and inside the jet cavity is markedly similar to that for Case 1. However, as will be discussed later, there are some qualitative changes in the jet velocity profile which point towards a trend with increasing slot height.

Case 3 (Re_δ= 0 , *h/d* =3 and *A/H* = 0.05). This quiescent flow case has half the diaphragm amplitude of Case 2 and consequently, half the nominal jet velocity. Figure 5 shows the contour plot of vorticity at four different stages in the cycle. It is observed that as the diaphragm moves into the expulsion strokes, a pair of vortices form and separate from the jet lip. However, as the diaphragm moves into the ingestion stroke, these vortices are still in the near vicinity of the slot and the effect of the flow generated near the jet lip during this phase tends to diminish the strength of these vortices. Consequently the train of strong, compact vortices observed in Case 1 is not observed here. Thus in order to form a train of convecting vortices, the vortex pair must be well separated from the jet lip at the initiation of the ingestion stroke. Although, it seems clear that this separation distance is dependant on the jet velocity as well as the induced velocity (and therefore strength) of the vortex pair, no simple criterion has yet been established for the formation of the vortex train.

Jet with External Crossflow

Case 4 (Re_δ= 260) This is the first case with an external crossflow. The boundary layer thickness Reynolds number of the external flow (Re_δ) is 260 and Figure 6 shows a sequence of vorticity contour plots for this case. It is observed that as in the case of quiescent external flow, a vortex pair forms at the jet lip during the expulsion stoke. However this vortex pair immediately comes under the influence of the crossflow and begins to convect downstream. As the axis of the vortex–pair rotates clockwise, the clockwise vortex (that formed from the right lip of the slot) moves toward the wall and consequently slows down. On the other hand the counter-clockwise vortex, which is exposed to a higher speed flow, convects downstream rapidly and approaches the clockwise vortex formed in the previous cycle. These two vortices now form a pair which moves vertically due to self-induction while continuously being convected downstream. It should be pointed out that $V_{\max}^{inv}/U_\infty \approx 3$ for this case. Thus even through the jet velocity is much higher than the crossflow velocity, the dynamics of the jet formation is significantly affected by the crossflow.

Case 5 (Re_δ = 1200). In this case, the boundary layer Reynolds number is increased to 1200 with an accompanying increase in the freestream velocity such that $V_{\max}^{inv}/U_\infty \approx 0.67$. Figure 7 shows the sequence of vorticity contour plots for this case and significant differences between this case and the previous cases are observed. First unlike the previous cases, the flow in the cavity is highly non-symmetric about the vertical centerline. Furthermore the vortical structure formed inside the cavity are stronger and consequently the region of almost–stagnant is smaller. During expulsion, two sets of counter rotating vortices are produced. However, due to the lower relative jet velocity, the vortices generated during expulsion do not penetrate out into the freestream. Furthermore, the counterclockwise rotating vortex is cancelled out by the boundary layer, which is comprised of clockwise vorticity. In contrast, the clockwise vortex entrains fluid from the boundary layer and from the freestream and grows in size as it convects downstream. In addition, another smaller clockwise vortex is formed which trails behind the primary vortex. The entrainment

of high momentum freestream fluid into the boundary layer by these vortices is an important feature since it has been hypothesized that this makes the resulting boundary layer more resistant to separation.

Case 6 (Re_δ **=** 2600**).** This case corresponds to the highest Reynolds number exterior flow simulated and for this simulation, $V_{\max}^{inv}/U_\infty \approx 0.3$. Figure 8 shows the sequence of vorticity contour plots for this case. With the higher exterior velocity, the counter-clockwise vorticity is cancelled quickly. Furthermore, the clockwise vortices are also found not to penetrate to the freestream side of the boundary layer. Consequently, no direct entrainment of freestream fluid into the boundary layer is observed. However as in the previous case, the primary clockwise vortex is followed by a smaller clockwise vortex. The formation of more than one vortex per cycle is indicative of the presence of a strong superharmonic component in the jet. This has implications for separation control since it implies that the jet is capable of providing a significant perturbation at twice the diaphragm frequency. It is also observed that the ingestion of higher momentum fluid energizes the fluid inside the cavity and consequently, the size of dead volume inside the cavity decreases. This further underscores the two ways coupling between the external flow and internal flow.

Jet Velocity Profiles

The spatial and temporal variation of the jet velocity determines all of the jet characteristic and therefore insight can be gained through detailed analysis of the jet profile. Figure 9 shows the jet exit velocity profiles for quiescent external flow cases as well as cases with an external crossflow. All plots correspond to the same diaphragm amplitude of A/H = 0.1. The four different lines in each plot represent four different stages in the cycle (similar to the vorticity plots) and the velocity in these plots has been normalized by $V_{\max}^{inv}$.

In Figure 9(a) are shown the jet velocity profiles for the quiescent external flow cases. Solid and dashed lines correspond to Cases 1 and 2 respectively. In both cases, the velocity profile is symmetric about the centerline of the jet. The first thing to note is the difference in the profile during the expulsion and ingestion stages. The velocity exhibits more of a "jet–like" profile during expulsion where the profile is more "plug–like" during ingestion. The normalized centerline velocity is about 1.4 at maximum expulsion and 1.0 at maximum ingestion. The profiles for the two cases are not significantly different. However, the more parabolic shape at peak expulsion for the higher value of h/d observed in Figure 9(a), represents a trend that becomes more apparent at higher values of this parameter.

Figure 9(b) shows the jet exit velocity profile for the Case 4 (Re_δ =260). Comparison with the profiles for the corresponding quiescent flow suggests a marked difference during the expulsion phase. In particular, both at maximum volume and maximum expulsion, the jet profile is skewed to the right In contrast, the jet profile is relatively unchanged during the ingestion stroke.

Figure 9(c) and (d) show the jet velocity profiles for Cases 5 and 6 with Re_δ=1200 and 2600 respectively. In general, the trend observed for Case 4 is also found to be present here. The jet is pushed to the right side of the slot due to the action of the external cross flow and this has two consequences. First, increased skewness of the jet to the right is observed with increasing Reynolds number of the external crossflow. Second, the effective area of the jet decreases and mass conservation then demands an increase in the jet velocity. The difference between the Re_δ =0 are Re_δ =1200 velocity profiles during the ingestion phase is somewhat less noticeable. Particularly at maximum ingestion, both flows exhibit almost plug like velocity profiles. However the trend towards increased skewness with Reynolds number is also observed in the ingestion phase.

The velocity profiles for Cases 5 and 6 are quite similar, and in order to explore this similarity, in Figure 10 we have compared the two sets of profiles where each profile has been normalized by its own peak expulsion velocity. The comparison indicates that the profile at the higher Reynolds number has a greater degree of skewness. Skewness in the velocity profile is dynamically important since it affects the enstrophy flux of the jet and the strength of the vortex structures expelled into the external flow. Thus, it might be appropriate to include some measure of skewness among the important characteristic features of the jet.

Jet Moment Coefficients

Figure 11 shows the momentum coefficient $\left(C^2\right)$ plotted versus A/H for Cases 1, 2, 5 and 6. In each plot, the momentum coefficient has been normalized by the momentum coefficient of the corresponding inviscid jet. Since our simulations indicate that the jet profile is markedly different during the expulsion and ingestion strokes, the momentum coefficient has been computed and plotted separately for these two phases. For the quiescent external flow cases (Figures 11 (a) and (b)), the normalized momentum coefficient of the expulsion stoke is greater than that of the ingestion stoke which is indicative of the jet–like velocity profile observed during expulsion. Furthermore, the values do not vary greatly with diaphragm amplitude and h/d, indicating that for at least the range of parameters studied here, the jet momentum flux scales in a simple manner with the inviscid jet velocity.

The cases with the external crossflow however show a markedly different behavior. While the momentum coefficient of the ingestion stroke is observed to asymptotically approach unity with increasing diaphragm amplitude for both cases, the momentum coefficient of the expulsion stroke is observed to increase continuously with this parameter. This clearly illustrates the advantage of separately analyzing the two phases of the jet cycle. It is also interesting to note that for the highest Reynolds number, the momentum coefficient of the expulsion stroke seems to saturate at high diaphragm amplitude where as a similar behavior is not observed for Re_δ=1200.

Virtual Aero–Shaping Effect

Finally, in Figure 12 we have plotted the streamlines corresponding to the mean flow. As mentioned earlier, some previous studies (Amitay et al. 1997, Chatlynne et al. 2001) have hypothesized that the synthetic jet is capable of altering the effective shape of the body by forming a mean recirculation zone in the external flow that is significantly larger than the size of the jet. To our knowledge, no direct support for this hypothesis has been provided in experiments or simulations. The current simulations provide us with an easy means of exploring this issue. In Figure 12 we compare the mean streamline pattern for three cases corresponding to Re_δ=260, 1200 and 2600 with *A/H* = 0.1. From Figure 12a, we see that the high relative velocity jet creates a relatively large system of recirculation bubbles on the surface of the flat plate with a length that is roughly 10*d*. On the other hand, for the lower velocity jets (Figure 12b and 12c), no recirculation zones are formed and the streamlines are just slightly perturbed only in the very near vicinity of jet exit. Thus, the synthetic jet is indeed capable of forming large mean recirculation zones. However this capability depends on the ratio of the jet to external flow velocity. For Re_δ=260, $V^{inv}_{\max}/U_\infty \approx 3$ whereas for Re_δ=1200 and 2600, this ratio is equal to 0.67 and 0.3 respectively. Thus, a large mean recirculation bubble forms only if the jet velocity is significantly higher than the external crossflow velocity. Recent simulations indicate that the parameter δ/d also has a significant influence on the size of the recirculation bubble but these results will be presented elsewhere.

4. CONCLUSIONS

Numerical simulations have been used to study the interaction of a synthetic jet with a flat plat boundary layer in a simplified, two-dimensional configuration. The diaphragm is modeled in a realistic manner as a moving boundary in an effort to compute the internal cavity flow accurately. The simulations show that the presence of the crossflow results in a significantly different flow as evidenced by the dynamics of the vortex structures produced by the jet and the jet velocity profiles. A systematic framework has been put forth for characterizing the jet in terms of the moments of the jet profiles. In addition to the moments, the simulations also indicate that skewness might be an important characteristic of the jet profile. Separate analysis of the ingestion and expulsion strokes is also found to be useful since it reveals a distinctly different jet behavior during these two phases for cases where there is an external crossflow. Finally, the so called virtual aero–shaping effect of the synthetic jet is investigated. It is found that large mean recirculation bubbles are formed in the external boundary layer only if the jet velocity is significantly higher than the crossflow velocity.

5. ACKNOWLEDGEMENTS

This work is supported partially by NASA Grant NAG–1–01024 monitored by Susan Gorton. Computer time has been provided by a startup grant from NCSA at the University of Illinois at Urbana-Champaign. We would also like to acknowledge extensive discussions with Professors L.N. Cattafesta and R.W. Mei during the course of this work.

6. REFERENCES

1 Amitay, M., Honohan, A., Trautman, M., Glezer, A. (1997). Modification of the Aerodynamic Characteristic of Bluff Bodies Using Fluidic Actuators. *AIAA 97–2004.*

2 Amitay, M., Smith, B. L., Glezer, A. (1998). Aerodynamic Flow Control Using Synthetic Jet Technology. *AIAA 98–0208.*

3 Chatlynne, E., Rumigny, N., Amitay, M. and Glezer, A. (2001). Virtual Aero–Shaping of a Clark–Y Airfoil Using Synthetic Jet actuators. *AIAA 2001–0732*.

4 Chen, Y., Liang, S., Aung, K., Glezer, A., Jagoda, J. (1999). Enhanced Mixing in a Simulated Combustor Using Synthetic Jet Actuators. *AIAA 99–0449*.

5 Crook, A., Sadri, A. M., Wood, N. J. (1999). The Development and Implementation of Synthetic Jets for the Control of Separated Flow. *AIAA 99–3176*.

6 Davis, S. A., Glezer, A. (1999). Mixing Control of Fuel Jets Using Synthetic Jet Technology : Velocity Field Measurement. *AIAA 99–0447*.

7 James, R. D., Jacobs, J. W., Glezer, A. (1996). A Round Turbulent Jet Produced by an Oscillating Diaphragm. *Phys. Fluids.* Vol. 8, No. 9.

8 Kral, L. D., Donovan, J. F., Cain, A. B., Cary, A. W. (1997). Numerical Simulation of Synthetic Jet Actuators. *AIAA 97–1824.*

9 Rizzetta, D. P., Visbal, M. R., Stanek, M. J. (1998). Numerical Investigation of Synthetic Jet Flowfields. *AIAA 98–2910*.

10 Seifert, A., Bachar, T., Wygnanski, I. (1998). Application of Active Separation Control to a Small Unmanned Air Vehicle. *Journal of Aircraft.* Vol. 36, No.2.

11 Seifert, A., Darabi, A., Wygnanski, I. (1996). Delay of Airfoil Stall by Periodic Excitation. *Journal of Aircraft.* Vol. 33, No. 4.

12 Smith, B.L., Glezer A. (1997). Vectoring and Small–scale Motions Effected in free Shear Flows Using Synthetic Jet Actuators. *AIAA 97–0213.*

13 Smith, D., Amitay, M., Kibens, V., Parekh, D., Glezer, A. (1998). Modification of Lifting Body Aerodynamics Using Synthetic Jet Actuators. *AIAA 98–0209*.

14 Udaykumar, H. S., Mittal R., and Shyy, W. (1999). Solid–Liquid Phase Front Computations in the Sharp Interface Limit on Fixed Grids. *J. Comput. Phys*. Vol. 18, pp. 535–574.

15 Udaykumar, H. S., Mittal R.,and Rampunggoon, P. (2000) Simulation of Solid–Fluid Interaction On Cartesian Grids. *Proc. of 2000 ASME Winter Annual Meeting*.

16 Ye, T., Mittal, R., Udaykumar, H. S., Shyy, W., (1999). An accurate Cartesian grid method for viscous incompressible flows with complex immersed boundaries. *J. Comp. Phys*. Vol. 156, pp. 209–240.

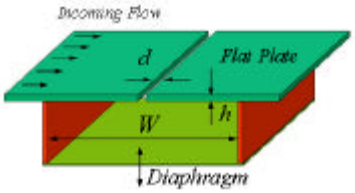

(a)

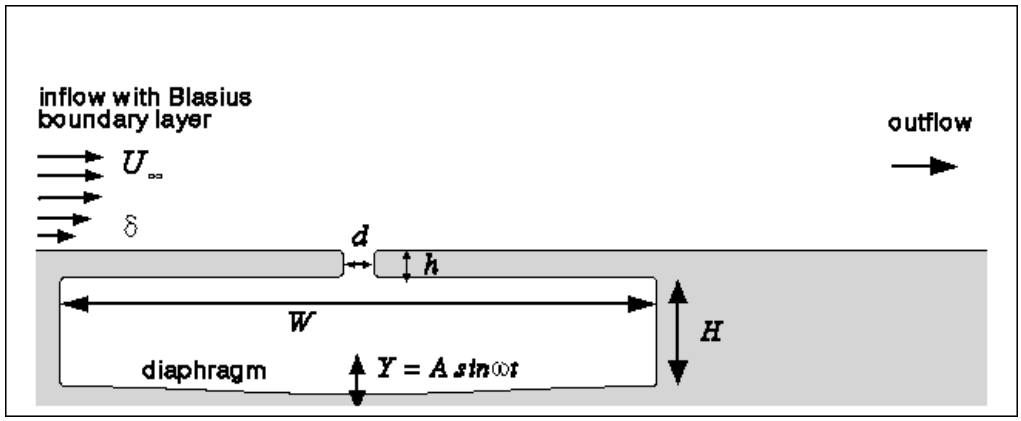

(b)

Figure 1. (a) Schematic diagram of a synthetic jet actuator with the rectangular chamber and slot. (b) The configuration of a 2–D synthetic jet used in the current study.

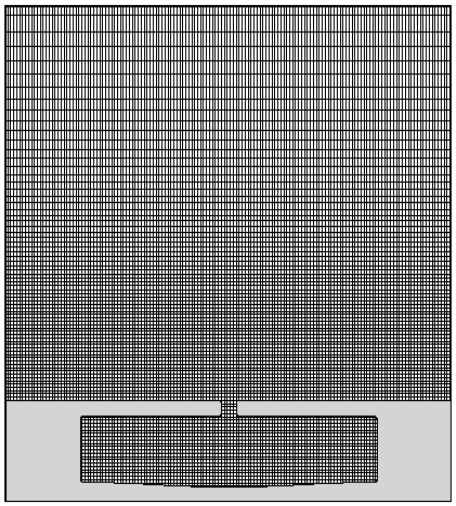

Figure 2. A fixed non–uniform Cartesian grid used in the synthetic jet calculation. Every third grid point is shown.

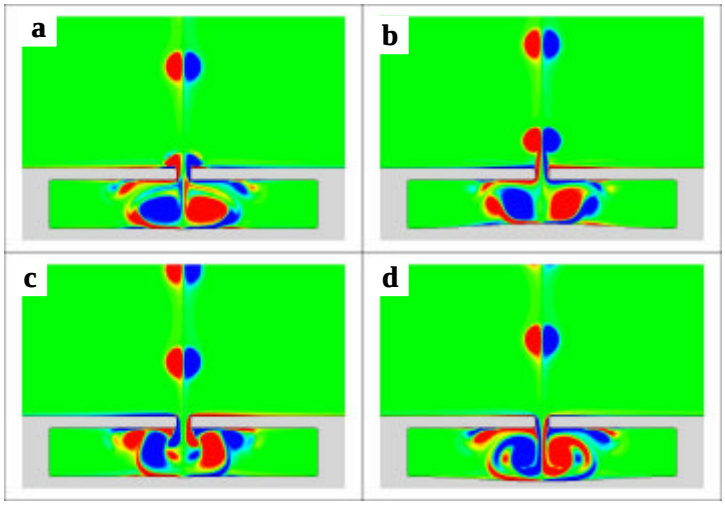

Figure 3. Plot of vorticity contour at four different stages for quiescent external flow, h/d=1 and A/H = 0.1. (a) Maximum expulsion (b) Minimum volume. (c) Maximum ingestion and (d) Maximum volume.

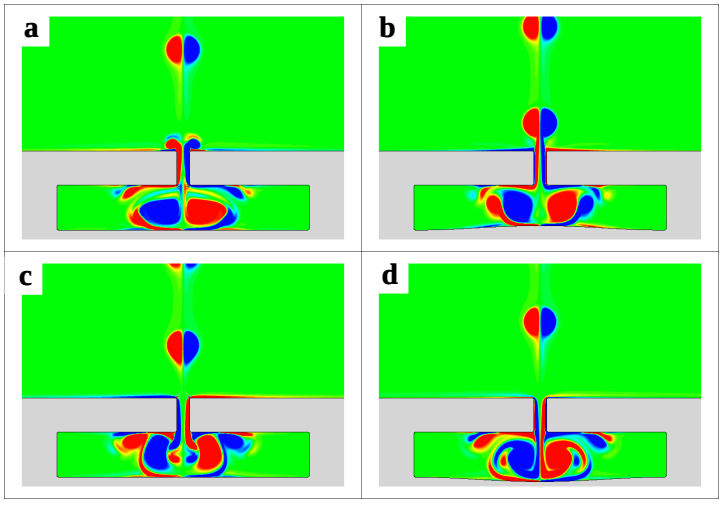

Figure 4. Plot of vorticity contour at four different stages for quiescent external flow, h/d=3 and A/H = 0.1. (a) maximum expulsion (b) minimum volume (c) maximum ingestion and (d) maximum volume.

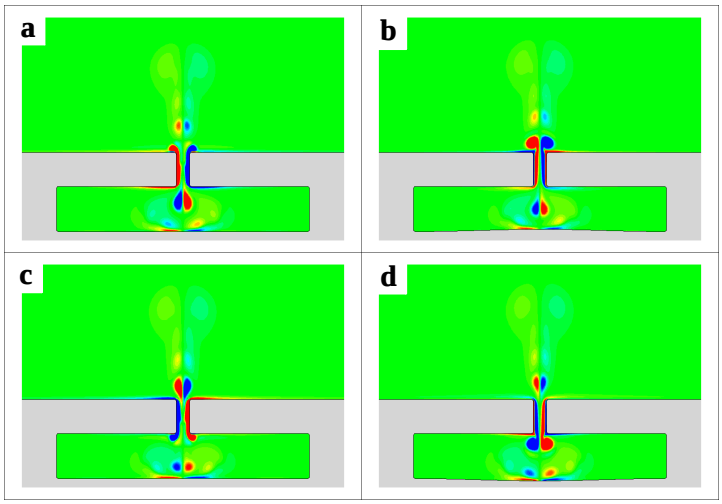

Figure 5. Plot of vorticity contour at four different stages for quiescent external flow, h/d=3 and A/H = 0.05. (a) maximum expulsion (b) minimum volume (c) maximum ingestion and (d) maximum volume.

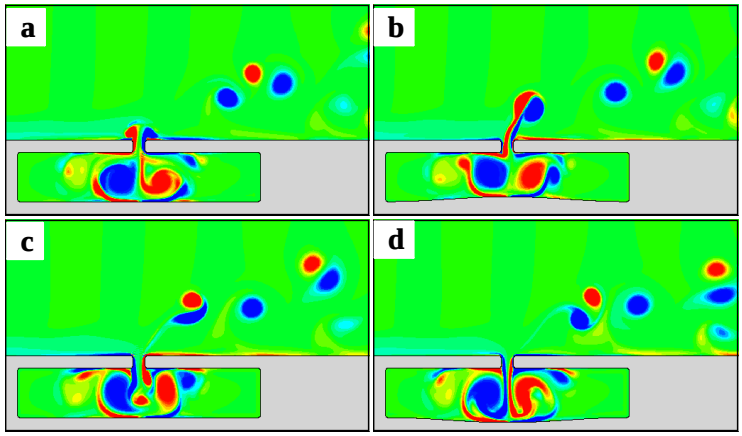

Figure 6. Plot of vorticity contour at four different stages for Re_d=260, h/d=1 and A/H = 0.1. (a) maximum expulsion (b) minimum volume (c) maximum ingestion and (d) maximum volume.

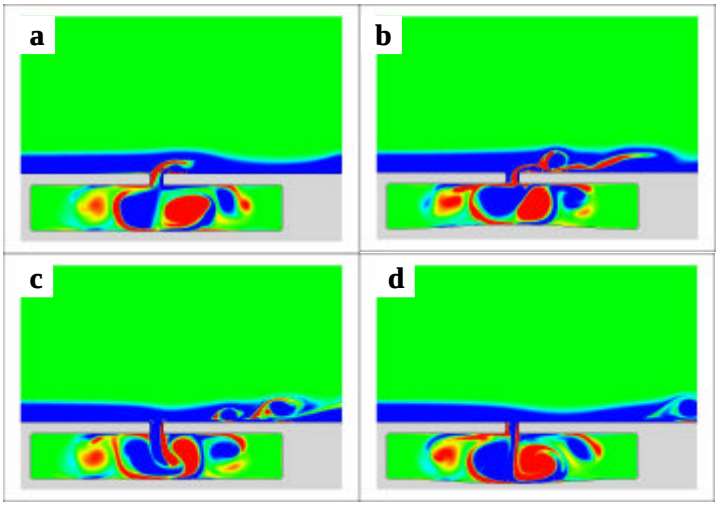

Figure 7. Plot of vorticity contour at four different stages for Re_d=1200, h/d=1 and A/H = 0.1. (a) maximum expulsion (b) minimum volume (c) maximum ingestion and (d) maximum volume.

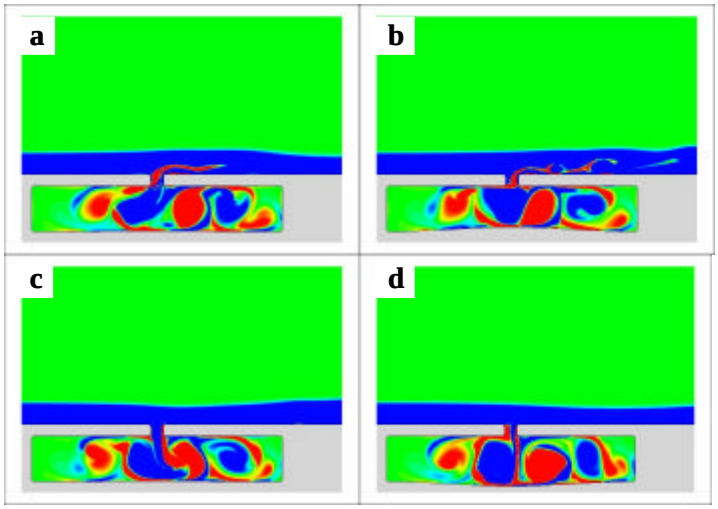

Figure 8. Plot of vorticity contour at four different stages for Re_d=2600, h/d=1 and A/H = 0.1. (a) maximum expulsion (b) minimum volume (c) maximum ingestion and (d) maximum volume.

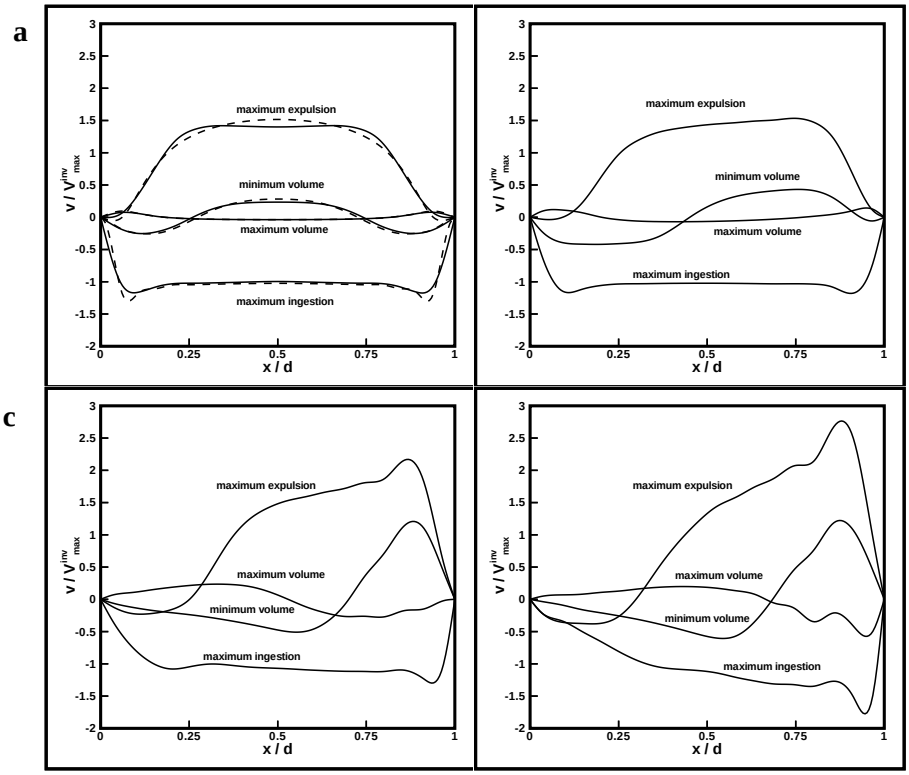

Figure 9. The velocity profile at the orifice exit. (a) quiescent external flow with h/d =1 shown as solid lines and *h/d* = 3 shown as dotted line. (b), (c) and (d) are for Re_δ =260, 1200 and 2600 respectively with *h/d* =1. Four different lines show four different stages.

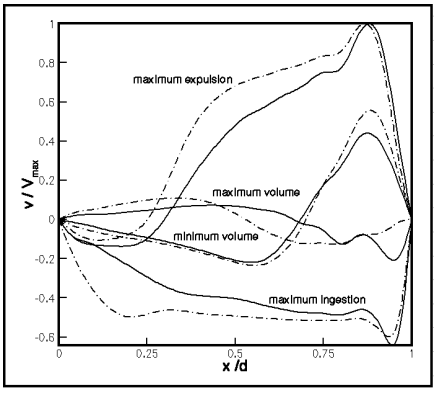

Figure 10. The velocity profile at the orifice exit normallized by its maximum value for Re_δ =1200 and 2600 with diaphragm amplitude *A/H*= 0.1. Re_δ=1200 case are shown with dotted line and Re_δ =2600 case are shown with solid lines.

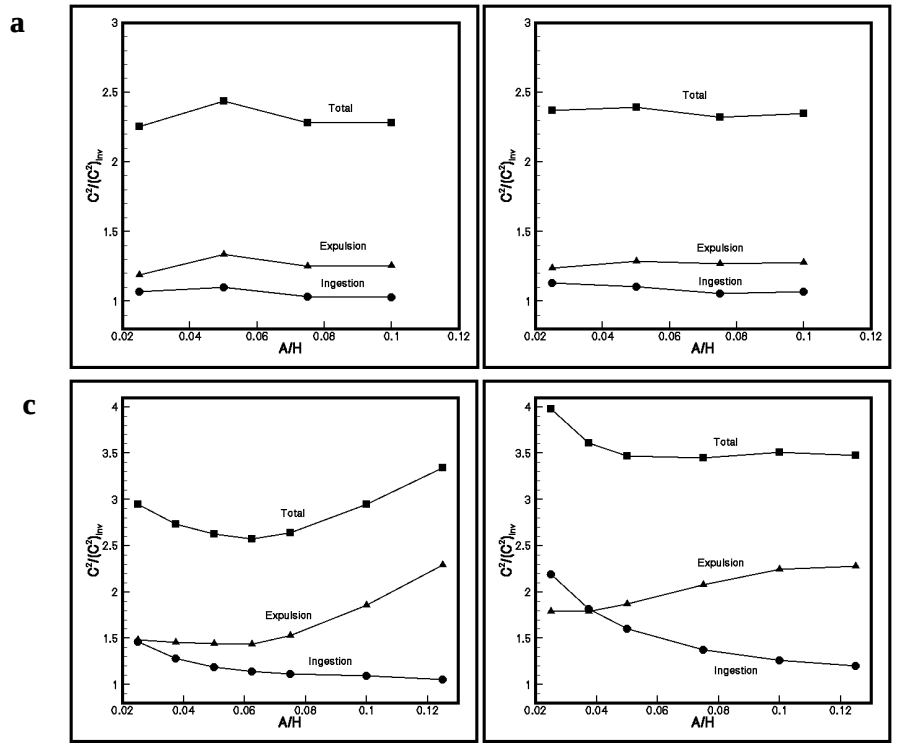

Figure 11. Momentum coefficient of the jet exit velocity profiles for (a)Re_d = 0, *h/d*=1 (b) Re_d = 0, *h/d*=3 (c) Re_d = 1200, *h/d*=1 (d)Re_d = 2600, *h/d*=1.

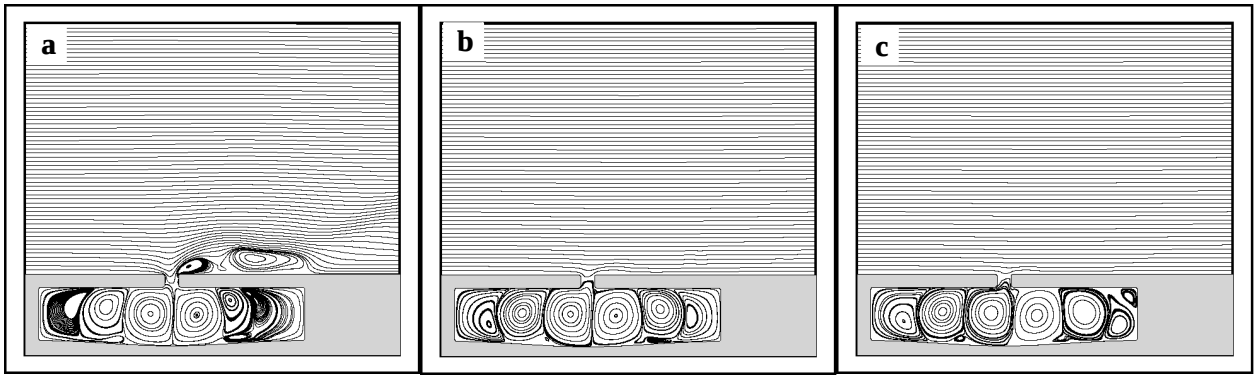

Figure 12. The mean streamline plot of the average velocity for the (a)Re_d =260 (b)Re_d =1200 (c) Re_d =2600 and *A/H*=0.1